Neutrino-heated winds from millisecond protomagnetars as sources of the weak *r*-process

Andrey D. Vlasov,[1]★ Brian D. Metzger,[1] Jonas Lippuner,[2] Luke F. Roberts[3]
and Todd A. Thompson[4]

[1]*Department of Physics and Columbia Astrophysics Laboratory, Columbia University, New York, NY 10027, USA*
[2]*TAPIR, Walter Burke Institute for Theoretical Physics, Mailcode 350-17, California Institute of Technology, Pasadena, CA 91125, USA*
[3]*NSCL and Department of Physics and Astronomy, Michigan State University, East Lansing, MI 48824, USA*
[4]*Department of Astronomy and Center for Cosmology and Astro-Particle Physics, The Ohio State University, Columbus, OH 43210, USA*

ABSTRACT

We explore heavy element nucleosynthesis in neutrino-driven winds from rapidly rotating, strongly magnetized protoneutron stars ('millisecond protomagnetars') for which the magnetic dipole is aligned with the rotation axis, and the field is assumed to be a static force-free configuration. We process the protomagnetar wind trajectories calculated by Vlasov, Metzger & Thompson through the *r*-process nuclear reaction network SkyNet using contemporary models for the evolution of the wind electron fraction during the protoneutron star cooling phase. Although we do not find a successful second or third-peak *r*-process for any rotation period P, we show that protomagnetars with $P \sim 1$–5 ms produce heavy element abundance distributions that extend to higher nuclear mass number than from otherwise equivalent spherical winds (with the mass fractions of some elements enhanced by factors of $\gtrsim 100$–1000). The heaviest elements are synthesized by outflows emerging along flux tubes that graze the closed zone and pass near the equatorial plane outside the light cylinder. Due to dependence of the nucleosynthesis pattern on the magnetic field strength and rotation rate of the protoneutron star, natural variations in these quantities between core collapse events could contribute to the observed diversity of the abundances of weak *r*-process nuclei in metal-poor stars. Further diversity, including possibly even a successful third-peak *r*-process, could be achieved for misaligned rotators with non-zero magnetic inclination with respect to the rotation axis. If protomagnetars are central engines for GRBs, their relativistic jets should contain a high-mass fraction of heavy nuclei of characteristic mass number $\bar{A} \approx 100$, providing a possible source for ultrahigh energy cosmic rays comprised of heavy nuclei with an energy spectrum that extends beyond the nominal Grezin–Zatsepin–Kuzmin cut-off for protons or iron nuclei.

Key words: magnetic fields – nuclear reactions, nucleosynthesis, abundances – stars: abundances – stars: magnetars – stars: rotation – supernovae: general.

1 INTRODUCTION

The astrophysical sites responsible for synthesizing the heaviest elements in the Universe via the rapid neutron capture process (*r*-process; Burbidge et al. 1957; Cameron 1957) have been debated for decades (for reviews, see Arnould, Goriely & Takahashi 2007; Qian & Wasserburg 2007; Sneden, Cowan & Gallino 2008; Thielemann et al. 2011).

Core collapse supernovae (SNe) have long been considered potential *r*-process sites. This is in part due to their short delays following star formation, which allows the earliest generations of metal-poor stars in our Galaxy (e.g. Mathews, Bazan &

Cowan 1992; Sneden et al. 2008), or satellite dwarf galaxies (e.g. Roederer 2017), to be polluted with *r*-process elements prior to significant iron enrichment. Throughout the 1990s, the high-entropy neutrino-heated winds from protoneutron stars (PNSs; Duncan, Shapiro & Wasserman 1986; Qian & Woosley 1996), which emerge on a time-scale of seconds after a successful explosion as the PNS deleptonizes, were considered the most likely *r*-process site[1] within the core collapse environment (e.g. Meyer et al. 1992; Woosley et al.

---

[1] Another *r*-process mechanism in the core collapse environment results from *ν*-induced spallation in the He shell (e.g. Banerjee, Haxton & Qian 2011). This channel is limited to very low metallicity $Z \lesssim 10^{-3}$ and thus cannot represent the dominant *r*-process source over the age of the Galaxy, though it could be important for the first generations of stars.

★ E-mail: vlasov@phys.columbia.edu

1994). A high entropy, or correspondingly low density, results in an α-rich freeze-out of the three- and effective four-body reactions responsible for forming seed nuclei in the wind (Woosley & Hoffman 1992). The resulting higher ratio of neutrons to seed nuclei then allows neutron captures to proceed to heavier elements than if the protons were instead entirely trapped in heavy seeds.

However, some contemporary (e.g. Takahashi, Witti & Janka 1994) and many subsequent calculations of the wind properties (e.g. Qian & Woosley 1996; Kajino et al. 2000; Otsuki et al. 2000; Sumiyoshi et al. 2000; Thompson, Burrows & Meyer 2001; Arcones, Janka & Scheck 2007; Roberts, Woosley & Hoffman 2010; Fischer et al. 2012; Martínez-Pinedo et al. 2012; Roberts, Reddy & Shen 2012) showed that the requisite combination of low electron fraction $Y_e \lesssim 0.5$ and high entropy needed to reach the second or third r-process peaks (Hoffman, Woosley & Qian 1997) were unlikely to be reached. Possible ways to get successfull r-process include a very massive PNS (Cardall & Fuller 1997), or given the presence of additional wind heating by damping of convectively excited acoustic or Alfvén waves (Suzuki & Nagataki 2005; Metzger et al. 2007) or of non-standard physics, such as an eV-mass sterile neutrino (e.g. Tamborra et al. 2012; Wu et al. 2014).

If all SNe produced the r-process in equal quantities, the required mass of r-process elements per event to explain Galactic abundances is relatively low, $\sim 10^{-5}$ M$_\odot$ (e.g. Macias & Ramirez-Ruiz 2016). However, several lines of evidence instead support much 'higher yield' r-process events being common in our Galaxy, both now and in its early history. These include the detection of ^{244}Pu on the ocean floor at abundances roughly two orders lower than that expected if the source were frequent, low-yield events like those predicted from PNS winds in normal SNe (Hotokezaka, Piran & Paul 2015; Wallner et al. 2015). Studies of ^{244}Pu abundance in meteorites confirm this conclusion (Tsujimoto, Yokoyama & Bekki 2017). A fraction of the stars in the dwarf galaxy Reticulum II are highly enriched in r-process elements, indicating that this galaxy was polluted early in its history by a single r-process event with a yield much higher than the standard neutrino-driven wind (Ji et al. 2016). Based on an analysis of the mass swept up by the SN blast wave, Macias & Ramirez-Ruiz (2016) argue that, in order to explain the largest enhancements in [Eu/Fe] at low metallicites, individual r-process events must synthesize at least $10^{-3.5}$ M$_\odot$ of r-process material, again significantly higher than predicted by standard PNS wind models. Such high abundances, if present in young Galactic SN remnants, would be detectable by their radioactive gamma-ray or X-ray decay lines (Qian, Vogel & Wasserburg 1998; Ripley et al. 2014).

Increasingly, the mergers of compact binary neutron star (NS) systems are seen as promising alternative sites for at least the heaviest r-process elements (Lattimer & Schramm 1974; Eichler et al. 1989; Freiburghaus, Rosswog & Thielemann 1999). General relativistic hydrodynamical simulations of the merger events show that some of the matter ejected dynamically during the merger retains a sufficiently low electron fraction ($Y_e \lesssim 0.1$) to form the heavy r-process elements extending beyond the third r-process peak at atomic number $Z \gtrsim 78$ (e.g. Goriely, Bauswein & Janka 2011; Wanajo et al. 2014).

Less clear in the merger framework is the origin of the charged particle process nuclei[2] ($Z = 38$–40) and of the 'light' or 'weak'

r-process nuclei ($Z \approx 41$–55). It is well known that r-process nuclei with $Z \lesssim 56$ in metal-poor stars show greater star-to-star variation in their abundance patterns than the heavier r-process nuclei (e.g. Honda et al. 2006; Roederer et al. 2010), despite showing an apparently robust pattern similar to the solar abundances in the heavier range $56 \lesssim Z \lesssim 76$ (e.g. Sneden et al. 2008). Such abundance variations are again difficult to explain from standard PNS winds, which, other than due to usually modest variations in the PNS mass, should produce broadly similar yields for each SN. This has motivated considering alternative sources for the light r-process nuclei in the environments of NS mergers, such as accretion disc winds (Fernández & Metzger 2013; Perego et al. 2014; Just et al. 2015; Martin et al. 2015; Wu et al. 2016) or components of the dynamical ejecta with higher electron fractions (Wanajo et al. 2014; Goriely et al. 2015).

This paper focuses on another variation on the canonical picture of neutrino-driven wind that occurs if the PNS is formed rapidly rotating, with an ultrastrong magnetic field $B \gtrsim 10^{14}$–10^{15} G, similar to those of Galactic magnetars (a so-called millisecond protomagnetar; Thompson 2004). If magnetic fields are dynamically important during the SN explosion itself, magnetic acceleration of matter away from the PNS can act to lower the asymptotic electron fraction of the unbound ejecta by preventing the outflowing matter from coming into equilibrium with neutrino absorption reactions (Metzger, Thompson & Quataert 2008b), possibly facilitating a heavy r-process (Metzger, Quataert & Thompson 2008a; Winteler et al. 2012; Nishimura, Takiwaki & Thielemann 2015; Nishimura et al. 2017). Although such models have great potential, quantitative studies of magnetohydrodynamics (MHD)-SNe are still in their infancy (e.g. Takiwaki, Kotake & Suwa 2016). High-resolution three-dimensional simulations are needed to resolve the dynamo responsible for tapping into the shear kinetic energy to generate a large-scale magnetic field (Guilet & Müller 2015; Mösta et al. 2015; Sawai & Yamada 2016). They are also needed to capture the growth of non-axisymmetric (e.g. magnetic kink and sausage mode) instabilities, which can disrupt MHD jet-like structures that otherwise are stable in axisymmetric simulations (e.g. Mösta et al. 2014). The observed rate of presumably MHD-powered, hyperenergetic SNe is also low compared to the total core collapse rate (e.g. Podsiadlowski et al. 2004), thus requiring a high r-process yield per event to explain the Galactic abundances through this channel alone.

Even if rotation and magnetic fields are not dynamically important during the explosion phase itself, they will become so during the subsequent neutrino-wind phase (Thompson 2004; Thompson, Chang & Quataert 2004; Metzger, Thompson & Quataert 2007). Indeed, such a situation is potentially much more common than a full-blown MHD-powered SN because the angular momentum of the progenitor stellar core needed to produce a PNS rotating with a period of $P \gtrsim 3$–4 ms is probably lower than that needed to explode the star (although see Thompson, Quataert & Burrows 2005). Furthermore, the impact of such a moderately rapidly rotating magnetar on the properties of the explosion, such as its total energy and ^{56}Ni yield, could be comparatively modest (e.g. Suwa & Tominaga 2015). The total birth rate of Galactic magnetars is estimated to exceed 10 per cent of the total core collapse rate (Woods & Thompson 2006), but the birth rotation rates are largely unconstrained observationally. A small population of core collapse SNe with extremely high optical luminosities may result from millisecond magnetar birth (e.g. Kasen & Bildsten 2010; Woosley 2010; Metzger et al. 2014). However, the limited range of rotation periods and surface dipole magnetic field strengths that result in greatly

---

[2] These elements are sometimes also referred to as light element primary process nuclei (Arcones & Montes 2011).

enhanced SN emission imply that only a fraction of all magnetar births manifests this way.

Vlasov et al. (2014, hereafter V14) solved for the steady-state structure of neutrino-heated winds from rotating, magnetized PNS, building on the previous one-dimensional equatorial monopole calculations of Metzger et al. (2007). V14 assumed that the magnetic field structure was that of an axisymmetric aligned dipole under the force-free approximation (Timokhin 2006; for schematic picture, see fig. 1). This is valid provided that the energy density of the magnetic field greatly exceeds that of the gas pressure and the kinetic energy density, as they find to be valid throughout the radii where the most important nucleosynthesis occurs for surface dipole field strengths of $B_d \gtrsim 10^{14}$–10^{15} G, depending on the neutrino luminosity (V14, their fig. 3). V14 obtained a series of one-dimensional solutions calculated along flux tubes corresponding to different polar field lines. They stitched together these flux tube solutions to determine the global wind properties across the entire open magnetosphere at a fixed neutrino luminosity and rotation period.

V14 found that protomagnetars with rotation periods of $P \sim 2$–3 ms produce outflows more favourable for the production of third-peak r-process nuclei. This is due to their much shorter expansion times τ_{dyn} through the seed nucleus formation region, yet only moderately lower entropies s, as compared to spherical non-rotating PNS winds. They found that the critical ratio of s^3/τ_{dyn} was higher than for spherical winds, but not sufficiently so that nucleosynthesis would proceed to the third r-process peak at $A \sim 200$, based on the analytic criteria of Hoffman et al. (1997). Except in the case of extremely rapid rotation, near the centrifugal break-up period of $P \sim 1$ ms, magnetic acceleration was not found to significantly enhance the mass outflow rate per unit surface area. In fact, the total mass-loss rate $\dot{M}$ is in most cases substantially lower than in an otherwise equivalent spherical wind because outflows occur only along open magnetic field lines, which thread only a small fraction ($\lesssim 10$ per cent, depending on the rotation period) of the total PNS surface.

This paper explores the nucleosynthetic yield of magnetar birth in greater detail by processing the wind trajectories from V14 through the nuclear reaction network SkyNet (Lippuner & Roberts 2015) in order to determine the detailed wind abundance pattern (Section 2). Even in the non-rotating spherical case, several critical wind properties remain uncertain; most notably the electron fraction Y_e depends sensitively on the differences between the luminosities and mean energies of the electron neutrinos and antineutrinos diffusing out from the PNS interior. The accuracy of these luminosities and neutrino energies is currently limited by uncertainties in the radiation transport and microphysics. Thus, in most cases we focus on comparing our calculated yields to those of otherwise equivalent spherical winds, in order to isolate the diversity in the nucleosynthesis imprinted exclusively by magnetorotational effects (Section 3). Although we find that protomagnetars are probably incapable of synthesizing the heaviest r-process elements, at least during the neutrino wind phase, their winds may still contribute to the inferred Galactic diversity of weak r-process sources (Section 4.2).

Beyond their role as possible sources of r-process nucleosynthesis and engines for powering luminous SNe, millisecond magnetars are contenders for the central engines powering gamma-ray bursts (GRB; Usov 1992; Wheeler et al. 2000; Thompson et al. 2004; Metzger et al. 2011a). If GRBs are indeed powered by the rotational energy of a magnetar, then the nucleosynthesis products of their winds will be directly entrained in the relativistic jet that escapes from the star and powers the prompt gamma-ray emission. As

we describe in Section 4.3, this unique jet composition could have implications for the composition of ultrahigh energy cosmic rays (UHECRs) if they are accelerated in GRB jets (Metzger, Giannios & Horiuchi 2011b).

2 NUCLEAR REACTION NETWORK CALCULATIONS

2.1 Thermodynamic trajectories

In the limit of force-free electrodynamics, the geometric structure of the protomagnetar wind from aligned rotator is fully specified by the magnetar rotation period P and the Y point radius R_Y, which defines the intersection between the last open field lines of the polar cap and the equatorial plane. We operate under the assumption that R_Y equals the radius of the light cylinder, $R_L = c/\Omega = cP/(2\pi)$, where $\Omega = 2\pi/P$ is the magnetar rotational angular frequency (Fig. 1). Unbound outflows occur along open magnetic flux bundles, with the outflow geometry varying with latitude θ from the pole at $\theta = 0$ to the last open field line at $\theta = \theta_{max} \simeq \sin^{-1}[R_{ns}/R_L]$, where $R_{ns} = 12$ km is the assumed NS radius.

Our nucleosynthesis calculations are performed along steady-state, one-dimensional wind trajectories for different field lines θ, as calculated by V14 for different values of P and electron neutrino luminosity $L_\nu \equiv (L_{\nu_e} + L_{\bar{\nu}_e})/2$, where L_{ν_e} and $L_{\bar{\nu}_e}$ are the neutrino and antineutrino luminosities, respectively. As described below, the results for different flux tubes are combined by integrating across the entire open magnetosphere, $\int_0^{\theta_{max}} \langle...\rangle d\Omega$, to quantify the total nucleosynthesis of the wind as a function of P and L_ν. The steady-state approximation we adopt is valid if the magnetosphere
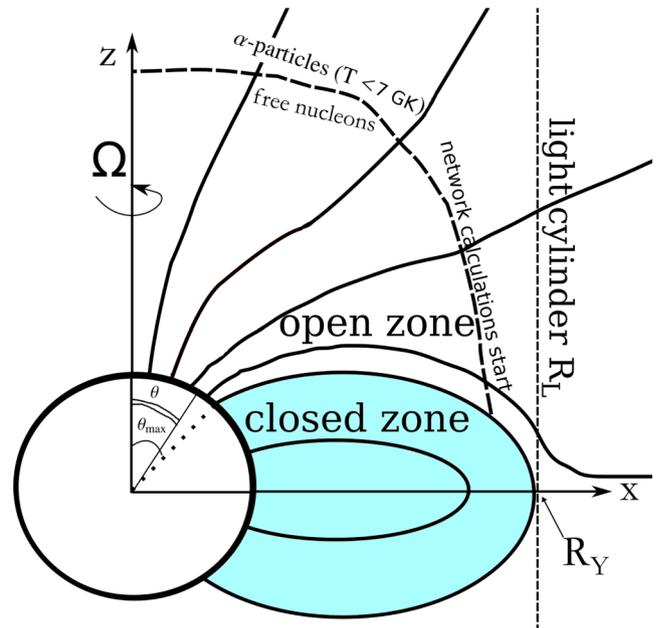

Figure 1. Geometry of neutrino-heated winds from magnetized aligned rotating PNSs. Outflows occur from the 'open zone', along field lines with polar angles $\theta < \theta_{max}$, where $\theta_{max} = \sin^{-1}[R_{ns}/R_Y]$ is the angle of the last closed field line, R_{ns} is the PNS radius, $R_Y \lesssim R_L$ is the radius at which the last closed field line crosses the equator (the 'Y point'), $R_L = c/\Omega$ is the light cylinder radius and Ω is the angular rotation rate of the PNS. In the illustration and in our calculations, we have assumed that $R_Y = R_L$. The network calculations start once the nucleons in the wind partially recombine to α-particles, at $T = 7 \times 10^9$ K.
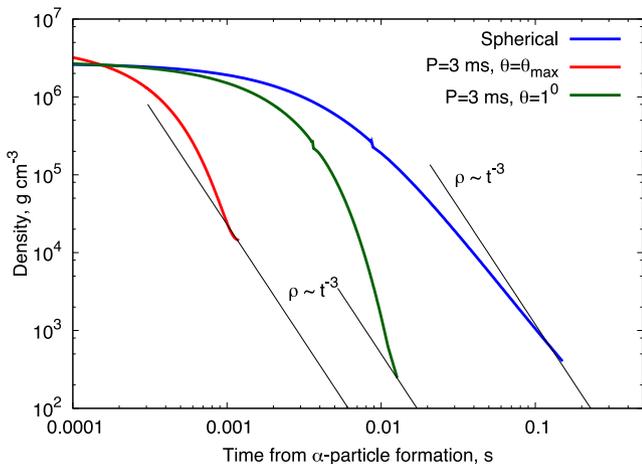
Figure 2. Density profiles of wind calculations from V14 for $L_\nu = 10^{52}$ erg s^{-1}, for both rotating protomagnetars with $P = 3$ ms (blue and green lines) and spherical wind (blue line). At large radii, we extrapolate the density profile $\rho \propto t^{-3}$ (black lines), as expected at very late times for homologous expansion.

Figure 3. Density $\rho(r)$ as a function of the radial coordinate r along the outflow in the neutrino-heated wind of a protomagnetar with a rotation period $P = 2$ ms and neutrino luminosity $L_\nu = 10^{52}$ erg s^{-1} (V14). Green and red lines show outflows along polar field lines ($\theta = 0$) and the last open field line ($\theta = \theta_{\max}$), while a purple line shows for comparison the trajectory of an otherwise identical spherical wind of the same neutrino luminosity. Also shown is the point of maximal specific heating (asterisk), approximate location of α-particle formation ($T = 0.5$ MeV; circle), the sonic point (diamond), and the light cylinder (square).

structure does not change with rotation or due to changes in the convective structure of the star. The time-scale for the outflow to pass through the nucleosynthesis region is much shorter than the time-scale over which L_ν is decreasing due to the Kelvin–Helmholtz cooling evolution of the NS or the time-scale over which P is increasing due to angular momentum losses due to magnetic dipole spin-down.

We start our reaction network calculations just after free nucleons recombine into α-particles at a temperature of $T \simeq 7 \times 10^9$ K. At small radii, where the magnetic field is dynamically strong compared to the thermal or kinetic energy densities, the force-free approximation is valid and we employ density trajectories from V14. At sufficiently large radii, matter inertia comes to dominate the energy density of the magnetic field, and the outflows should approach a spherical outflow. The density profile of a steady-state wind that has reached a constant asymptotic velocity should approach $\propto 1/r^2 \propto 1/t^2$, while at larger radii where internal velocity gradients become important the profile will approach $\rho \propto 1/r^3 \propto 1/t^3$ appropriate for a freely expanding homologous outflow. As shown in Fig. 2, we interpolate directly between the V14 trajectories at small radii and the asymptotic $1/t^3$ dependence at large radii. This simplification is motivated by the fact that the qualitative features of the abundance patterns are robust to the detailed density trajectory outside of the radii where charged particle processes cease and the neutron-to-seed ratio has been determined. In order to test the importance of an alternate density extrapolation, we have run a handful of trajectories with $\rho \propto 1/r^2$ extrapolation. The difference in the asymptotic abundances between the $1/r^3$ and $1/r^2$ density profiles is less than 1 per cent for most cases, and none of the conclusions of this paper are changed.

Another simplification is that we neglect heating or deceleration of the wind by the reverse shock, which is produced as the wind interacts with the surrounding SN ejecta. This is justified in part[3] because the radius of the pulsar wind termination shock $R_{rs} \simeq (v_{ej}/c)^{1/2} R_{ej}$ (e.g. Gaensler & Slane 2006), where v_{ej} is the mean

velocity of the SN ejecta, is generally much larger than the radius where the formation of seed nuclei occurs. The latter generally occurs close to the light cylinder radius, which determines the radial scale of outflow divergence. At time t since explosion, we have $R_{ej} \simeq v_{ej} t$ and thus

$$\frac{R_{rs}}{R_L} \approx 37 \left(\frac{v_{ej}}{10^4 \, \mathrm{km \, s^{-1}}} \right)^{3/2} \left(\frac{t}{1 \, \mathrm{s}} \right) \left(\frac{P}{1 \, \mathrm{ms}} \right)^{-1}. \quad (1)$$

We thus have $R_{rs} \gg R_L$ for times $t \gtrsim 1$ s and rotation periods $P \lesssim 10$ ms of interest, implying that seed formation occurs well inside the termination shock.

We start the nucleosynthesis network after the formation of α-particles. By this time, most of the key parameters of the outflow (entropy s, expansion time-scale τ_{dyn}, electron fraction Y_e and mass-loss rate $\dot{M}$) have already been determined in the free nucleon zone at small radii, where nuclear statistical equilibrium (NSE) provides a good approximation for equation of state. Furthermore, after α-particle formation, neutrino heating and cooling have become negligible and hence are not included in the network reactions. Fig. 3 shows that our calculations begin at radii five to seven times larger than the location where the neutrino heating rate reaches its maximum just above the NS surface. The locations of maximum neutrino heating are marked by stars in this figure, while the locations where $T = 0.5$ MeV, which approximately corresponds to the locations of α-formation, are marked by circles.

V14 do not account for entropy gain from α-particle formation, which we therefore increase by hand from its initial value s_0 from V14 according to

$$s = s_0 + X_\alpha(s, \rho, Y_e) \Delta s_\alpha, \quad (2)$$

where $X_\alpha(s, \rho, Y_e)$ is the mass fraction of α in NSE with given entropy and Y_e, $\Delta s_\alpha = Q_\alpha / T_\alpha$ is the entropy gain from α formation, Q_α is the heat of α-formation and T_α is the temperature of α formation. Since the latter depends weakly on other wind parameters, we adopt a fixed value of $\Delta s_\alpha = 10 k_B$ nucleon^{-1}, corresponding to $T_\alpha = 8$ GK. The starting temperature for the reaction network is determined from the density and the entropy according to

---

[3] In addition, highly magnetized winds experience much weaker compressional heating than unmagnetized winds due to the additional support from magnetic pressure.
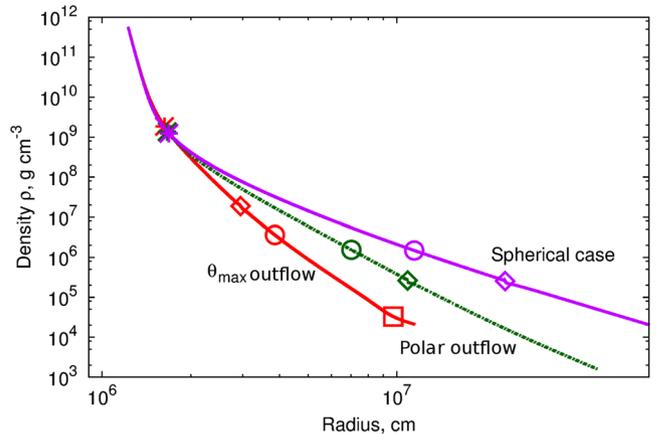
equation (2), with subsequent evolution tracked self-consistently from the density trajectory and radioactive heating.

Finally, we must specify the initial outflow electron fraction used in our network calculations, which equals the 'final' electron fraction $Y_{e,\text{final}}$ set by processes near the PNS surface. In standard thermally driven PNS winds, this value is determined by the competition between electron neutrino and electron antineutrino capture reactions on free nucleons,

$$\nu_e + n \leftrightarrow p + e^- \qquad \bar{\nu}_e + p \leftrightarrow n + e^+. \qquad (3)$$

These reactions have frozen-out (become slow compared to the expansion rate) at the large radii where our calculations would begin, resulting in an electron fraction close to the equilibrium value set by neutrino absorption reactions (Qian & Woosley 1996)

$$Y_{e,\text{eq}} = \left(1 + \frac{L_{\bar{\nu}_e}}{L_{\nu_e}} \frac{\langle \varepsilon_{\bar{\nu}_e} \rangle - 2\Delta + 1.2\Delta^2/\langle \varepsilon_{\bar{\nu}_e} \rangle}{\langle \varepsilon_{\nu_e} \rangle + 2\Delta + 1.2\Delta^2/\langle \varepsilon_{\nu_e} \rangle}\right)^{-1}, \qquad (4)$$

where $\Delta = 1.293$ MeV is proton–neutron mass difference and $\langle \varepsilon_{\bar{\nu}_e} \rangle / \langle \varepsilon_{\nu_e} \rangle$ are the mean energies of electron neutrinos and antineutrinos, respectively.

For relatively slowly rotating protomagnetars, $P > 2$ ms, the final electron fraction is very similar to the normal thermally driven case, i.e. $Y_{e,\text{final}} \simeq Y_{e,\text{eq}}$. However, in the most rapidly spinning cases, $P \lesssim 2$ ms, we can have $Y_{e,\text{final}} < Y_{e,\text{eq}}$ due to rapid magnetocentrifugal acceleration (Thompson et al. 2004; Metzger et al. 2007, 2008b, V14), which causes a premature freeze-out of the neutrino absorption processes before Y_e is raised completely from its low value near the PNS surface. More quantitatively, introducing the definition $(\Delta Y_e)_{\text{cent}} \equiv Y_{e,\text{final}} - Y_{e,\text{eq}}$, we find that maximum $(\Delta Y_e)_{\text{cent}} \simeq -0.14$ for $P = 1$ ms, $L_\nu = 6 \times 10^{51}$ erg s^{-1}, $\theta = \theta_{\text{max}}$ and $(\Delta Y_e)_{\text{cent}} \simeq -0.011$ for $P = 2$ ms, $L_\nu = 10^{52}$ erg s^{-1}, $\theta = \theta_{\text{max}}$. We keep the dependence of $(\Delta Y_e)_{\text{cent}}$ on $L_\nu = 0.5(L_{\nu_e} + L_{\bar{\nu}_e})$ and θ and we neglect the dependence on the other parameters ($Y_{e,\text{eq}}, L_{\nu_e}, \varepsilon_{\nu_e}, \varepsilon_{\bar{\nu}_e}$). As the initial conditions for our network calculations we therefore take $Y_{e,\text{final}} = Y_{e,\text{eq}}(t) + (\Delta Y_e)_{\text{cent}}[L_\nu, \theta]$ for $P = 1, 2$ ms and $Y_e = Y_e^{\text{eq}}(t)$ for all other periods.

The value of $Y_{e,\text{eq}}(t)$ is calculated from equation (4) using the time evolution of $L_{\nu_e}, L_{\bar{\nu}_e}, \langle \varepsilon_{\bar{\nu}_e} \rangle, \langle \varepsilon_{\nu_e} \rangle$ from PNS cooling calculations of Roberts et al. (2012). Given the uncertainties in neutrino radiation transport (e.g. Fischer et al. 2012; Martínez-Pinedo et al. 2012; Roberts et al. 2012), especially in the essentially unexplored case of very rapid rotation (however, see Thompson et al. 2005; Thompson 2007) and given the effects of ultrastrong magnetic fields on the microphysics (Lai & Qian 1998; Duan & Qian 2004), we concentrate on comparing the properties rotating protomagnetar winds to the conventional unmagnetized spherical wind case.

2.2 Reaction network calculations

We start our nucleosynthesis calculations at the point where V14 trajectory reaches $T = 7 \times 10^9$ K, corresponding to the approximate temperature of α-particle formation. However, our actual starting temperature is slightly larger because of the entropy enhancement from α-formation (equation 2). We use the nuclear reaction network SkyNet (Lippuner & Roberts 2015) for the nucleosynthesis calculation. The composition starts out in NSE, a good approximation for the initial temperature $T \gtrsim 7 \times 10^9$ K. Given the extrapolated density as a function of time (see Section 2.1), SkyNet then evolves the abundances of 7843 nuclear species under the influence of over 140 000 nuclear reactions. The evolved species range from free

neutrons and protons to ^{337}Cn ($Z = 112$). SkyNet also evolves the entropy and temperature, which change due to the expansion of the material and energy released by the nuclear reactions. SkyNet uses a modified version of the Helmholtz equation of state (Timmes & Swesty 2000), which treats every nuclear species as a separate Boltzmann gas, also including electron–positron gas with arbitrary degree of relativism and photon gas. In some trajectories, the initial temperature after taking into account the entropy gain from α-formation is above 10^{10} K. In these cases, SkyNet uses NSE for evolution of the network up to 10^{10} K, below which it switches to full network evolution with all reactions.

The rates of the strong reactions come from the JINA REACLIB data base (Cyburt et al. 2010), but only the forward rates are used and the inverse rates are computed from detailed balance. This is to ensure consistency with NSE, which depends on the nuclear masses. Spontaneous and neutron-induced fission rates are taken from Frankel & Metropolis (1947), Panov et al. (2010), Mamdouh et al. (2001), and Wahl (2002). Most of the weak rates come from Fuller, Fowler & Newman (1982), Oda et al. (1994) and Langanke & Martínez-Pinedo (2000) whenever they are available, and otherwise the REACLIB weak rates are used. We used the nuclear masses and partition functions from the WebNucleo XML file distributed with REACLIB, which contains experimental data where available and finite-range droplet macroscopic model (see e.g. Moller et al. 2016) data otherwise.

For $Y_e > 0.5$, charged particle process nuclei ($Z \simeq 38$–40) can also be formed through νp process (e.g. Fröhlich et al. 2006; Arcones & Montes 2011); however, even though SkyNet supports including neutrino interactions, we do not include these in the present calculations. We leave an exploration of charged particle process nucleus formation in proton-rich protomagnetar winds to future work.

2.3 Classes of abundance models

The nucleosynthesis products of protomagnetar winds vary as a function of the latitude of the open flux tube at a fixed time. They also vary in a global sense, integrated over the entire magnetosphere at a fixed time or averaged over all times in the PNS cooling evolution. We cover the range of possible diagnostics of the wind nucleosynthesis by calculating the abundance patterns in three general cases.

(i) Individual flux tubes along different latitudes θ at a fixed time (or equivalently, neutrino luminosity), producing abundance yields as a function of (θ, L_ν, Y_e, P).

(ii) The entire wind at a fixed time, by integrating individual flux tubes over the solid angle of the open magnetosphere, producing abundance yields as a function of (L_ν, Y_e, P).

(iii) The entire wind (integrated over the open magnetosphere) averaged over the Kelvin–Helmholtz cooling epoch $L_\nu(t)$ (Fig. 4), producing abundance yields as a function of just the rotation period P.

In the angle-integrated cases, we weight the abundances by the mass-loss rate along each given open flux tube. In the time-integrated case, they are also weighted by the total ejected mass from the entire magnetosphere at each epoch t. In the latter case, by fixing the rotation period, we have assumed that the magnetic spin-down time of the pulsar is longer than Kelvin–Helmholtz cooling time-scale of seconds; this approximately is justified for surface magnetic dipole field strengths of $B_d \lesssim 10^{16}$ G.

In the time-integrated case, we also consider two methods for treating the time evolution of the electron fraction Y_e. In one case,
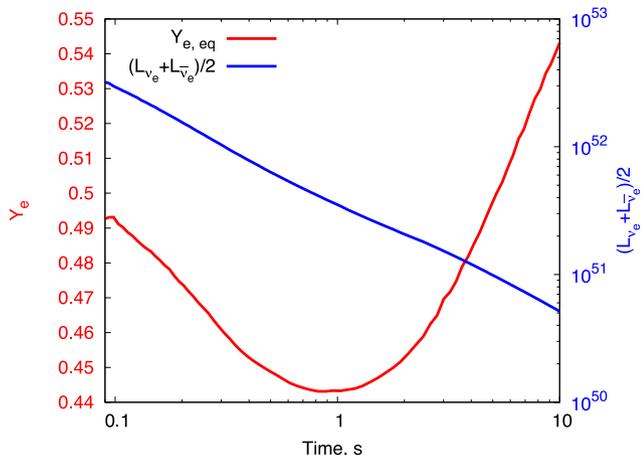
Figure 4. The blue line (right axis) shows the time evolution of the electron neutrino luminosity $L_\nu(t) = (L_{\nu_e} + L_{\bar{\nu}_e})/2$ used in our calculations, based on the electron neutrino luminosity $L_{\nu_e}(t)$ and antineutrino luminosity $L_{\bar{\nu}_e}(t)$ from the Kelvin–Helmholtz cooling calculations of Roberts et al. (2012). A red line (left axis) shows the corresponding equilibrium value of the electron fraction $Y_{e,\,eq}$ (equation 4) used as input to our nucleosynthesis calculations (we also down-correct Y_e for centrifugal effects for $P \leq 2$ ms, but this is not shown here).

Table 1. Summary of time-integrated models.

P, ms	$\bar{A}^a$	$\bar{Z}^a$	X_α	X_n^b	X_p^b	$M_{\rm ej}$, M$_\odot$
$-^c$	87.34	37.71	0.561	9.24×10^{-7}	3.65×10^{-7}	9.98×10^{-4}
1	98.94	42.61	0.429	4.83×10^{-4}	5.58×10^{-5}	3.45×10^{-3}
2	98.73	42.53	0.685	3.42×10^{-4}	4.07×10^{-5}	1.79×10^{-4}
3	97.81	42.13	0.719	2.18×10^{-4}	2.55×10^{-5}	1.06×10^{-4}
4	97.36	41.94	0.714	1.90×10^{-4}	2.22×10^{-5}	7.80×10^{-5}
5	95.07	40.96	0.688	1.62×10^{-4}	1.90×10^{-5}	6.64×10^{-5}
10	94.07	40.53	0.675	9.34×10^{-5}	1.08×10^{-5}	2.52×10^{-5}

Notes. ^{a}Mean mass number for all elements except H and He.
^{b}Mass fraction of free neutrons and free protons at $t = 100$ s, i.e. prior to the decay of free neutrons.
^{c}Spherical solutions.

we fix Y_e at a constant value throughout the cooling epoch. In the second case, we derive its value as described in Section 2.1 using the equilibrium electron fraction (equation 4) from the time evolution of L_ν, $L_{\bar{\nu}}$, $\langle \varepsilon_{\bar{\nu}_e} \rangle$, $\langle \varepsilon_{\nu_e} \rangle$ from the PNS cooling calculations of Roberts et al. (2012), as shown in Fig. 4. Since we are focused on the r-process, we integrate only over epochs when $Y_{e,\,eq} < 0.5$, i.e. at times $0.1 \lesssim t \lesssim 5$ s, and all reported wind properties (e.g. ejecta mass, mass fractions, etc. – all the data in Table 1) refer to just this time period. This is a reasonable approximation to the total yield of the wind since the bulk of the total mass-loss occurs at early times $t \sim 1$–2 s.

3 RESULTS

3.1 Variation in wind properties across the magnetosphere

Based on the $s^3/\tau_{\rm exp}$ threshold criterion of Hoffman et al. (1997), V14 concluded that rotating protomagnetars are more suitable for producing heavy r-process nuclei than in the spherical wind case, but not to the degree necessary to reach the third abundance peak ($Z \gtrsim 78$) for currently favoured values of $Y_e \gtrsim 0.4$. Although our

nucleosynthesis calculations presented here confirm this broad conclusion, we find some quantitative differences. While V14 found that the most promising rotation period for producing heavy elements was $P = 2$ ms, here we find that $P = 1$ ms is instead optimal.[4] $P = 1$ ms is a special case because centrifugal effects are particularly pronounced, and the values of s and $Y_{e,\,\rm final}$ thus differ significantly from the spherical case.

We focus our analysis in this section on models with $P = 1$ and 3 ms. The latter case plays important role because the rotational energy of the magnetar with $P = 3$ ms, $E_{\rm rot} = I\Omega^2/2 \approx 10^{51}$ erg, is comparable to the kinetic energy of a normal SN. Hence, magnetars born with $P \gtrsim 3$ ms could in principle be 'hidden' among the normal population of normal SNe without violating constraints on the observed kinetic energies of their ejecta from SN spectra and the total energies of their remnants (as already discussed, hypernovae are known to be rare; e.g. Podsiadlowski et al. 2004; Woosley & Bloom 2006).

Fig. 5 shows the mass fraction as a function of nuclear charge Z for different outflow latitudes θ, calculated for $P = 1$ ms (top panel) and $P = 3$ ms (lower panel). For all values of θ, the abundance distribution extends to higher masses Z than the otherwise equivalent spherical wind with the same L_ν and Y_e, which is shown for comparison with a purple line. Part of this effect is due to the shorter expansion time through the seed formation region caused by the faster diverging outflow of a real function $\propto 1/r^3$ in the dipole magnetic field, as compared to the spherical wind case (a real function $\propto 1/r^2$), as well as centrifugal force from rotation.

Fig. 5 also shows that the abundance distribution proceeds to heavier elements with increasing θ due to the additional acceleration caused by magnetocentrifugal acceleration along field lines inclined with respect to the rotation axis. The heaviest nuclei are synthesized in those outflows that graze the closed zone and pass near the equatorial plane outside the light cylinder.

Shown for comparison with a dashed blue line are the abundances integrated over the open zone of the entire magnetosphere, from which it is apparent that the flow properties near the last open field line ($\theta_{\rm max}$) also dominate the total abundance of the wind. This is expected because outflows with larger θ contribute a greater fraction of the total open solid angle of the magnetosphere and, to a lesser extent, because the mass-loss rate per unit surface area is enhanced by magnetocentrifugal acceleration for larger θ (Thompson et al. 2004; Metzger et al. 2007).

Most of our calculations employ Newtonian gravity for an NS of mass $M = 1.4\,{\rm M}_\odot$. However, Fig. 6 shows the results for a more massive NS with $M = 2\,{\rm M}_\odot$ NS, as well as for a model with $M = 1.4\,{\rm M}_\odot$ but using the Paczyński–Wiita potential to mimic the effects of general relativity (GR). The effect of a higher NS mass, or the *effectively* higher mass due to the deeper Paczyński–Wiita potential, is also to increase the maximum mass nuclei synthesized, extending it up to $Z \approx 54$ (Xenon), near the peak of the second r-process peak. This well-known effect results because of the additional heating, and hence higher asymptotic entropy, achieved by the winds to escape from the deeper potential well (Cardall & Fuller 1997). Note, however, that we have not included the GR-induced gravitational redshift on the mean neutrino energies, which somewhat reduces the neutrino heating rate and acts to mitigate this effect (e.g. Thompson et al. 2001).

---

[4] $P = 1$ ms is also the most promising period if we use the modified Hoffman et al. (1997) criterion for $Y_e < 0.38$ where appropriate.
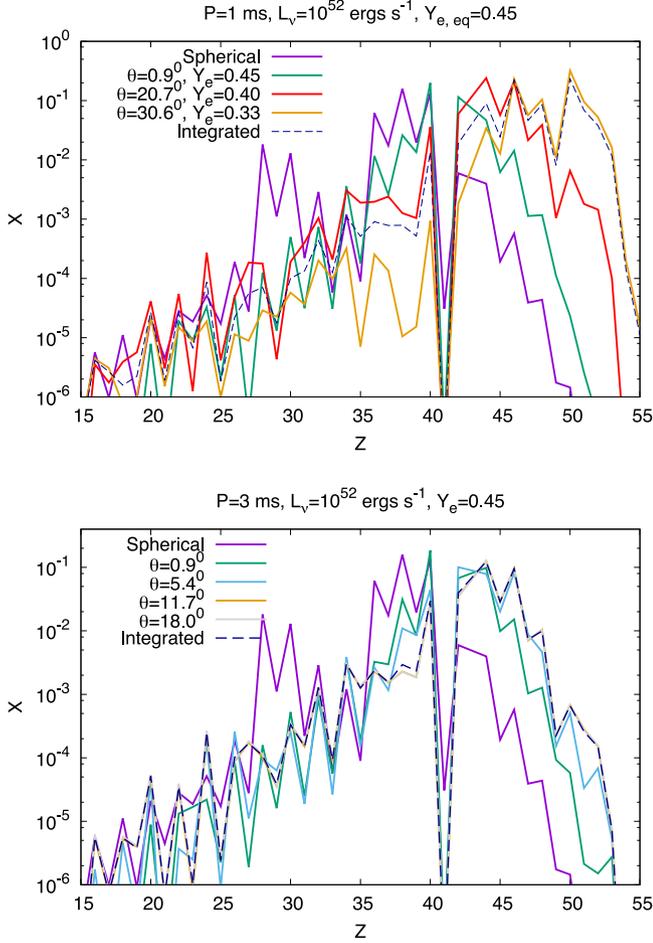
Figure 6. Mass fraction of nuclei, integrated across the entire open magnetosphere of a protomagnetar with $P = 3$ ms, $Y_e = 0.45$, and $L_\nu = 10^{52}$ erg s^{-1}. Here, we compare the fiducial case of Newtonian gravity for a $1.4\,M_\odot$ NS (purple line) to the result for a $2.0\,M_\odot$ NS (blue line). Also shown is the case of a $1.4\,M_\odot$ NS (green line) calculated using a modified Paczyński–Wiita potential, meant to mimic the deeper potential well of GR.

Figure 5. Mass fraction of nuclei $X(Z)$ synthesized in the protomagnetar wind of neutrino luminosity $L_\nu = 10^{52}$ erg s^{-1} and neutrino equilibrium electron fraction $Y_e = 0.45$. Results are shown for two rotation periods: $P = 1$ ms (top panel) and $P = 3$ ms (bottom panel); in the former case, the value of Y_e is lower than its equilibrium value set by neutrino absorptions due to centrifugal acceleration effects, as marked in the key. Different lines correspond to the abundances synthesized in the wind along field lines with different polar angles θ at the NS surface, ranging from near the pole ($\theta \simeq 0$) to the last open field line $\theta_{\max}$ (depending on the rotation period). Shown for comparison with a blue dashed line are the mass-weighted abundances integrated over the solid angle of the open magnetosphere. A purple line shows the abundances from an otherwise identical calculation of a spherical non-rotating non-magnetized wind.

3.2 Time-integrated models

Fig. 7 shows the total yield of protomagnetar winds, integrated across the entire Kelvin–Helmholtz cooling evolution using the $Y_e(t)$ evolution from Roberts et al. (2012, Fig. 4) and $(\Delta Y_e)_{\mathrm{cent}}$ from V14 for $P = 1, 2$ ms. We show both the total mass (top panel) and the ratio of abundances to those calculated in the otherwise equivalent case of a spherical wind (bottom panel). One clear trend is that the abundance distribution extends to heavier elements in the rotating case, with a larger number of heavy elements synthesized with decreasing rotation period as compared to the otherwise equivalent spherical case.

However, strong magnetic fields also *reduce* the mass of the ejecta in light elements. This reduction is due to the fact that only a small fraction of the PNS surface is open to outflows, such that the total ejecta mass from each event is typically smaller than the spherical
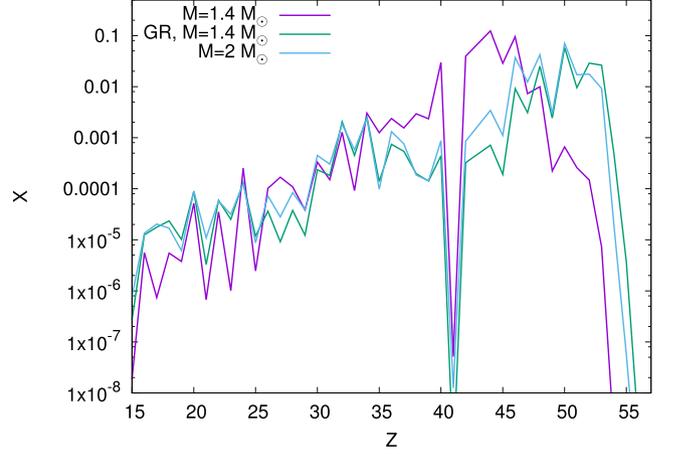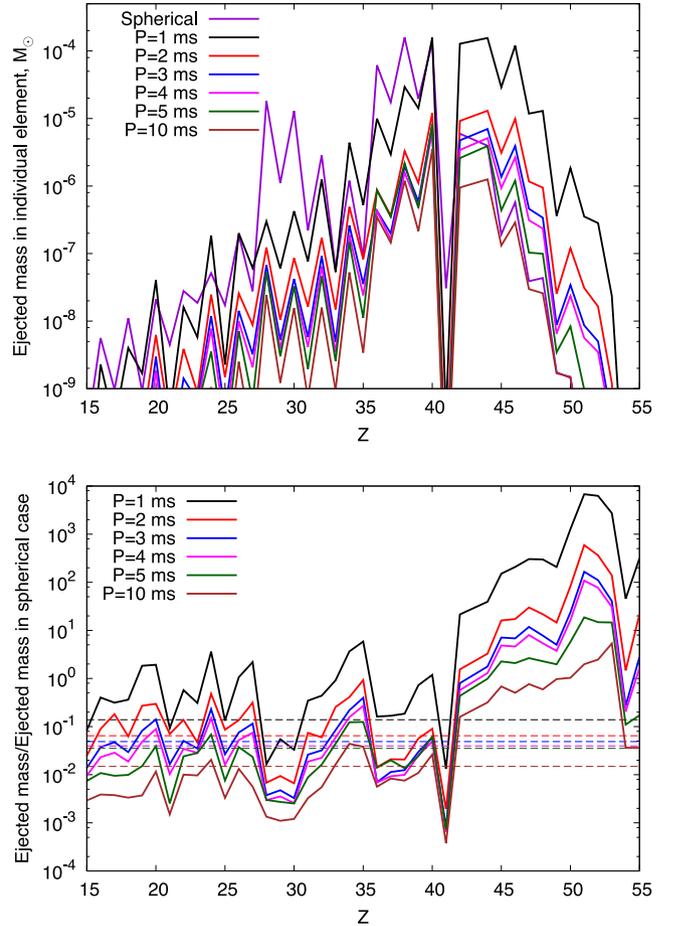

Figure 7. Top: total wind ejecta mass in individual elements, time-integrated across the Kelvin–Helmholtz cooling epoch using the $Y_e(t)$ evolution from Roberts et al. (2012, Fig. 4) and $(\Delta Y_e)_{\mathrm{cent}}$ from V14 for $P = 1, 2$ ms. Bottom: ratio of the wind ejecta mass of each element in protomagnetar models relative to those in the otherwise equivalent spherical non-rotating wind models. The dashed lines of same colour shows the purely geometric factor f_{open} (equation 5) arising from fraction of the PNS magnetosphere open to outflows.
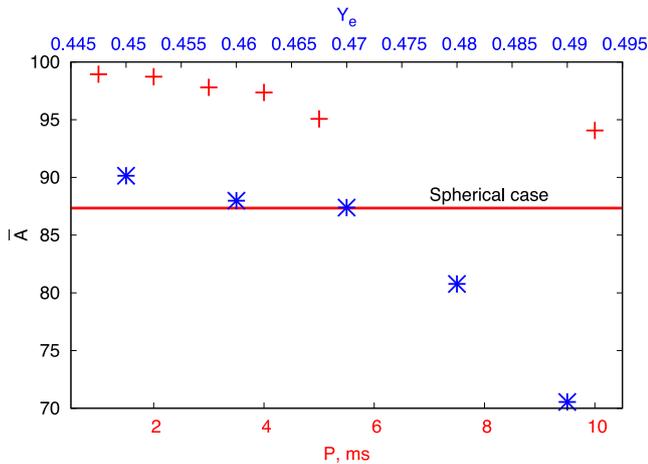
Figure 8. Abundance-weighted mass $\bar{A}$ of synthesized nuclei, excluding H and He. Bottom axis: red crosses show the results for time-integrated models with $Y_e(t)$ evolution from Roberts et al. (2012, Fig. 4) for different rotation periods, while the solid line shows the result for the non-rotating spherical wind case for the same Y_e evolution. Top axis: blue asterisks show time-integrated models of a spherical wind which instead assume a temporally constant value of Y_e as marked on the top axis.
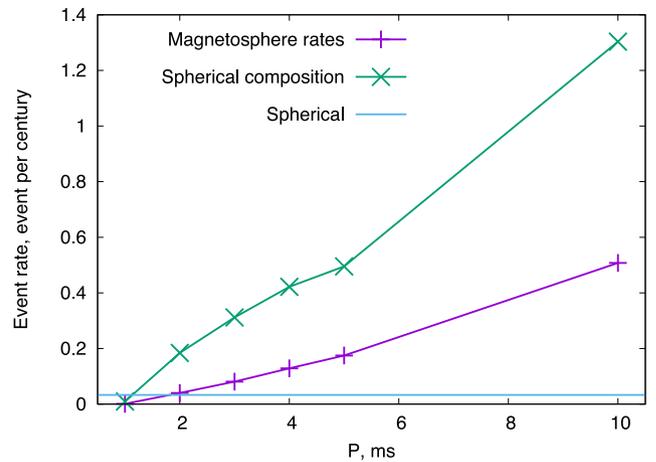

Figure 9. Upper limit on rates of magnetar birth as a function of the birth rotation period P so as not to overproduce Solar system abundances of r-process nuclei (equation 6). Purple crosses show the results based on our abundance calculations of protomagnetar winds (Fig. 7). Green crosses show the rate constraint that would result if we used the composition from the spherical model, but down-correcting the ejecta mass M_{ej} to account for the purely geometric correction f_{open} (equation 5) resulting from the small solid angle of the open magnetosphere.

case by this purely geometric factor of

$$f_{open} \approx \frac{2\pi\theta_{max}^2}{4\pi} \approx \frac{1}{2}\frac{R_{ns}}{R_Y} \approx 0.13 \left(\frac{P}{1\,\mathrm{ms}}\right)^{-1}, \qquad (5)$$

which we show as a dashed line in Fig. 7. The only period that exhibits a significant enhancement compared to this geometric factor across most elements is $P = 1$ ms because of the large centrifugal enhancement in the mass-loss rate per unit surface area, which overcomes the (comparatively modest) reduction due to $f_{open} \approx 0.1$ in this fastest spinning case.

Fig. 8 shows the abundance-weighted mass $\bar{A}$ of synthesized nuclei as a function of the magnetar rotation period (red crosses, bottom axis), from which it is clear that $\bar{A}$ decreases monotonically with increasing spin period P. For comparison, a red line shows the result for a spherical wind using the same neutrino-cooling evolution from Roberts et al. (2012) as in the magnetized case. The mean value of $\bar{A}$ for $P = 1\text{--}10$ ms is 97, but $\bar{A}$ in spherical case is $\bar{A}_{sph} = 87$; hence, the rotation with $P = 1\text{--}10$ ms lowers $\bar{A}$ by 10 units. On the top axis, we also show the value of $\bar{A}$ calculated in the spherical non-rotating case assuming a temporally *fixed* value of Y_e.

The fact that the ejecta mass in individual elements exceeds those produced in the spherical case by a factor up to 10^2 (or 10^3 in case of $P = 1$ ms) has the striking implication that millisecond magnetars possess unique nucleosynthetic signatures, which would be measurable even if only one in 100(1000) NSs were born strongly magnetized with $P \lesssim 4$ ms ($P \approx 1$ ms).

Table 1 summarizes important quantities from our time-integrated models. We see that centrifugal effects enhance the values of $\bar{A}$ and $\bar{Z}$ moving to shorter periods. Enhanced centrifugal mass-loss overpowers the geometric factor for $P = 1$ ms, such that the total ejecta mass of $M_{ej} \approx 3 \times 10^{-3}\,\mathrm{M}_\odot$ for $P = 1$ ms is about three times higher than in the spherical case.

4 DISCUSSION

4.1 Rate constraints on the birth of magnetars

If millisecond protomagnetars are found to produce large quantities of rare isotopes, one could in principle place constraints on their birth periods based on their nucleosynthetic yields compared to those in our Galaxy as inferred from the solar abundances. An upper limit on the birth rate of magnetars of a given rotation period is given by

$$R \leq \min \frac{X_{i,\odot}M_{gas}}{M_{ej,i}t} = \frac{X_{i,\odot}M_{gas}}{X_{i,wind}M_{ej}t_{gal}}, \qquad (6)$$

where $X_{i,wind}$ is the mass fraction of an element (or an isotope) in the PNS wind, M_{ej} is the total wind ejecta mass, $X_{i,\odot}$ is the mass fraction of the same element (or isotope) on the Sun, $M_{gas} \approx 3.3 \times 10^{10}\,\mathrm{M}_\odot$ is the total mass of gas in the Galaxy when the Sun formed, and $t_{gal} \approx 10^{10}$ yr is the age of the Galaxy when the Sun formed. In other words, the total ejecta mass of a given element or isotope under consideration cannot exceed the total mass of that element contained in the gas from which the Sun formed (assuming the Sun formed from 'ordinary' gas with abundances representative of the Galactic mean).

Fig. 9 shows the result of such a calculation of the maximum allowed birth rate in events per century, which is approximately also the fraction of NS births. A purple line shows the rate derived from our time-integrated calculation of protomagnetar winds as a function of the magnetar rotation period. Shown for comparison with a blue line is the rate limit for the standard non-rotating spherical wind case.

It may be surprising that, for standard spherical winds, the allowed event rate is very low, $\lesssim 0.05$ per century. This is due to the well-known fact that standard spherical winds overproduce the charged particle process nuclei with $Z = 38\text{--}40$ (e.g. Arcones & Montes 2011) for the neutron-rich wind conditions $Y_e \lesssim 0.5$ found using contemporary PNS cooling calculations (Fischer et al. 2012; Martínez-Pinedo et al. 2012; Roberts et al. 2012).

It may also be surprising that the rate constraints are weaker on protomagnetar winds than on spherical winds, despite the fact that the nucleosynthesis of protomagnetars extends to higher Z elements, which are rarer in the Solar system. This is again explained by the fact that only a small fraction of the PNS surface is open to outflows, such that the total ejecta mass from each event is typically smaller than the spherical case by the geometric factor f_{open} (equation 5). The green line in Fig. 9 shows the rate constraints one would derive if the composition of a spherical wind was attenuated by the purely geometric factor f_{open}. The resulting rate constraint is weaker than the protomagnetar case including the full effects of the magnetized wind dynamics on the composition itself (purple line); this shows that the rare higher Z elements that are synthesized protomagnetar winds do tighten the rate constraint significantly, but not enough to overcome the purely geometric suppression factor f_{open}.

The net result of all of this is that the effects of magnetic fields and rotation are sufficiently modest that – given also current uncertainties in the electron fraction of the wind – one cannot at present place meaningful constraints even on the birth rate of non-rotating PNS, much less on their birth periods and magnetic field strengths. Still, our results show that at least under our assumption for the electron fraction of the wind, the birth rate of magnetars *with millisecond periods* cannot exceed ∼1–10 per cent of the core collapse SN rate, depending on the rotation period. Reassuringly, this number exceeds the *total* birth rate of Galactic magnetars (Woods & Thompson 2006) and is consistent with the lower millisecond magnetar birth rate inferred if they power hydrogen-poor superluminous SNe (e.g. Quimby et al. 2013).

It is possible that NSs are generically born with magnetar-strength fields. This could occur, for instance, if strong fields are generated by a convective dynamo in the PNS, which later decay away in the majority of cases by the time they are observed as radio pulsars. We note that in such a case the reduction in the open fraction of the PNS surface due to confinement by a dynamically important magnetic fields (Thompson 2004) would be generic to all winds and thus could help alleviate the current overproduction of the charged particle process nucleus $Y_e < 0.5$ wind models (even if rapid rotation itself is comparatively rare). Also note that including GR will increase the depth of potential well for matter to escape and lower neutrino energy because of gravitational redshift. Both these factors will lower the ejecta mass, also alleviating constraints on the event rate.

4.2 As sources of light *r*-process nuclei in metal-poor stars

Fig. 10 shows the abundances of our time-integrated models (Fig. 7) compared to the abundances of two Galactic metal-poor stars, HD 122563 (Honda et al. 2006) and HD 88609 (Honda et al. 2007), that show a relative dearth of 'heavy' *r*-process nuclei ($Z \gtrsim 56$) compared to the Solar system; all abundances have been normalized to the Ru ($Z = 44$) abundance in our spherical model. Although the spherical wind models produce large quantities of charged particle process nuclei ($Z = 38$–40), they underproduce the solar abundances of the weak *r*-process nuclei ($Z = 41$–55) in HD 122563 and HD 88609. By contrast, our rotating magnetar models produce larger abundances of weak *r*-process nuclei with $Z \gtrsim 40$, while comparatively underproducing the lighter charged particle process nuclei.

Our results provide a potential explanation, within the PNS wind paradigm, for the fact that light *r*-process nuclei with $Z \lesssim 56$ in metal-poor stars show greater star-to-star variation than the heavier *r*-process nuclei (e.g. Roederer et al. 2010). We propose that such star-to-star variation could be understood if the charged particle
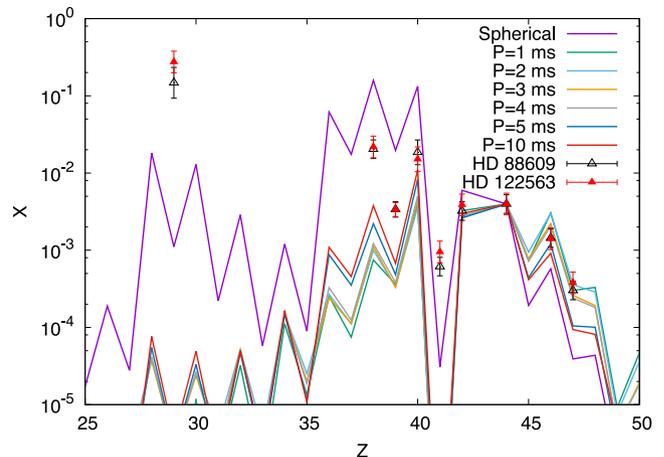

Figure 10. Abundances in time-integrated models compared to abundances of Galactic metal-poor stars HD 122563 (Honda et al. 2006) and HD 88609 (Honda et al. 2007). Abundances are normalized to the Ru ($Z = 44$) abundance of our spherical time-integrated model. After $Z = 55$, our models produce very small abundances and they are not able to match the abundances observed in HD 122563 and HD 88609.

process and weak *r*-process nuclei are produced by a combination of normal (slowly rotating and/or weakly magnetized) NSs and a subclass of magnetars with a range of birth rotation periods.

Magnetars with very short birth rotation periods of $P \lesssim 1$ ms have been discussed as a source of heavy *r*-process nuclei, mainly by the ejection of low-Ye matter by magnetocentrifugal acceleration in neutrino-heated winds (Metzger et al. 2007, Metzger et al. 2008b) and during the early dynamical phases of a bipolar explosion (Metzger et al. 2008b; Winteler et al. 2012; Nishimura et al. 2015). In this work, we do not consider dynamical ejection of matter, but rather the neutrino-heated wind of a rapidly rotating, but subcritical magnetar with $P = 1$ ms, our most promising case. Such rotation rates should occur more commonly than super break-up rotation periods. The rapid core rotation rates of the massive progenitor stars giving rise to millisecond protomagnetars are likely to be more common at the low metallicities that characterized early epochs in the chemical evolution of our Galaxy (Stanek et al. 2006). Studies of Galactic inhomogeneous evolution conclude that a source of *r*-process that sets in early in the history of star formation, like neutrino-heated winds from protomagnetars, is required to explain chemical evolution at low metallicities (Cescutti et al. 2015; Wehmeyer, Pignatari & Thielemann 2015).

Both this work and V14 focused on the winds from aligned protomagnetars, for which the rotation axis coincides with magnetic axis. Studies of the more general case of inclined rotators are less developed because the problem is inherently non-stationary (for review, see e.g. Cerutti & Beloborodov 2016). Numerical studies have shown that the equatorial region of the magnetar outflow in this case is characterized by 'stripes' of alternating magnetic fields, which are separated by current sheets and are prone to magnetic reconnection (e.g. Spitkovsky 2006). Dissipation of magnetic energy, for instance as these stripes reconnect outside the light cylinder radius (e.g. Lyubarsky & Kirk 2001), provides an additional possible source of heating in the wind, which would act as both to increase the entropy of the flow and contribute to its acceleration. If this heating occurs near the seed formation radius, typically close to the light cylinder in our models, this would substantially enhance the prospects for synthesizing third-peak *r*-process nuclei in misaligned rotators compared to the aligned case studied here. The magnetic

inclination angle therefore provides another parameter, in addition to the rotation period, which could impart diversity to the *r*-process yields of protomagnetar winds.

More work is clearly needed to distinguish the magnetar hypothesis from other proposed sites of the light *r*-process elements, such as binary NS mergers (Fernández & Metzger 2013; Perego et al. 2014; Wanajo et al. 2014; Goriely et al. 2015; Just et al. 2015; Martin et al. 2015; Wu et al. 2016).

4.3 GRB engines and UHECR sources

The birth of millisecond magnetars may also give rise to collimated relativistic jets, which in some cases are sufficiently powerful to break out of the progenitor stars and may power GRB (Usov 1992; Thompson et al. 2004; Bucciantini et al. 2008; Metzger et al. 2011a). The acceleration of relativistic particles due to shocks or magnetic reconnection within GRB jets is also considered a promising source for the origin of UHECRs (Waxman 1995). If the outflows from millisecond magnetars indeed feed GRB jets, then the composition of the UHECRs accelerated within such a jet should contain a large quantity of heavy nuclei (Metzger et al. 2011b; see also Horiuchi et al. 2012).[5]

For rotation periods of $P \sim 1$–2 ms, the ratio of the Poynting flux luminosity to the baryon loading of the magnetar wind is sufficiently high so that the resulting jet could reach an asymptotic bulk Lorentz factor of $\Gamma \approx 100$–1000 (e.g.Thompson et al. 2004; Metzger et al. 2007). Metzger et al. (2011b) show that this is sufficient to produce the observed gamma-ray emission and to accelerate nuclei within the jet to ultrahigh energies $\gtrsim 10^{19}$ eV per particle. GRBs associated with magnetar birth therefore provide a natural explanation for the otherwise puzzling observation by the Pierre Auger Observatory that the highest energy UHECRs are composed of heavy nuclei instead of protons (Abraham et al. 2010; see however Abbasi et al. 2005). This model is also consistent with constraints on the non-detection of high-energy neutrinos coincident with GRBs with IceCube (Abbasi et al. 2011) since nuclei typically lose energy through other processes than photo-pion production, and hence are not expected to be accompanied by a neutrino flux as large as that predicted for proton-dominated compositions.

Fig. 11 shows that the composition of protomagnetar jets is predicted to be roughly $X_{He} \approx 0.6$ by mass in helium, with the remainder $X_h \simeq 1 - X_{He} \approx 0.4$ in heavy nuclei of average mass $\bar{A} \approx 95$ (Fig. 8, Table 1). The latter result is non-trivial because if the expansion time of the outflow were sufficiently short then neutron capture reactions could in principle freeze-out with an order unity mass fraction of free neutrons. However, we find that the free neutron mass fraction at 100 s is always small $X_n \lesssim 10^{-3}$ (Fig. 11). Such a low free neutron fraction would disfavour models in which the GRB prompt emission is powered by the relative kinetic energy in the jet between its neutral (neutron) and charged (protons, nuclei) constituents (Beloborodov 2010), unless the nuclei are destroyed in the jet by photodisintegration before the radius at which neutrons collisionally decouple (see below).

The prediction of UHECRs dominated by nuclei with $A \sim 100$ has important implications for the energy spectrum and pathlength
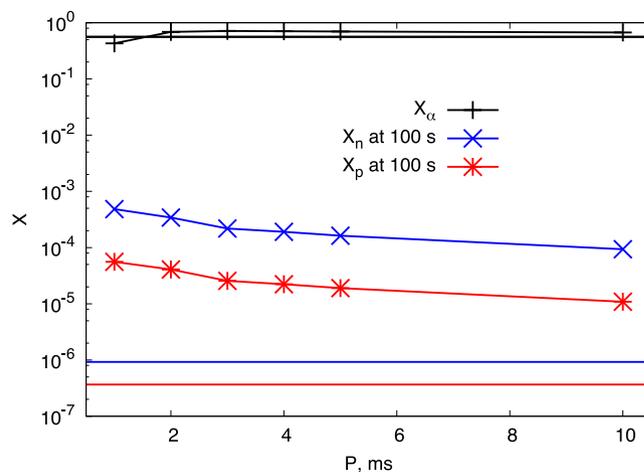
Figure 11. Time-integrated mass fractions of α-particles, free neutrons and free protons in protomagnetar winds. We report the mass fractions of neutrons and protons at $t = 100$ s, since at that time free neutrons have not yet decayed to protons. The horizontal lines of corresponding colours show these quantities in the spherical model. In spherical wind, the expansion is slower and hence neutrons have more time to capture on to seed nuclei during the *r*-process. This results in much lower value of X_n for spherical winds.

of UHECRs through the intergalactic medium. The normal Grezin–Zatsepin–Kuzmin (GZK) cut-off in the cosmic ray spectrum occurs due to inelastic pion production by high energy protons that interact with the cosmic microwave background (CMB) or extragalactic background light (Greisen 1966; Zatsepin & Kuzmin 1966). At a fixed (measured) cosmic ray energy E, a nucleus of mass A has a bulk Lorentz factor that is a factor of A times smaller than a proton of the same energy. Naively, one would therefore expect the effective GZK cut-off energy of a nucleus (interacting with background radiation of a fixed temperature like the CMB) to be A time larger than that for a proton. However, nuclei suffer from other loss processes, the most important one being giant dipole resonances (GDR), which once excited cause the nucleus to shed free nucleons or α-particles, reducing its energy.

Metzger et al. (2011b) show that a nucleus of initial mass $A = 56A_{56}$ and energy $E = 10^{20}E_{20}$ eV travels a distance of

$$\chi_{75} = 170E_{20}^{-1.5}A_{56}^{1.3}\bar{n}_{ej}^{-1} \quad \text{Mpc} \tag{7}$$

before losing 25 per cent of its initial energy, where $\bar{n}_{ej}^{-1} \approx 1$ is the mean number of nucleons ejected per GDR excitation. For an iron nucleus, the mean free path with respect to EBL interaction is coincidentally the same as mean free path for protons with respect to CMB pair production, resulting in a similar GZK cut-off to the proton case. However, $\chi_{75} \propto A^{1.3}$ implies that for $A = 95$ nuclei from our models (Fig. 8), the mean free path is two times larger than for protons. Thus, we expect the GZK-like cut-off in the cosmic ray energy spectrum to extend farther for protomagnetar wind composition than the usual cut-off predicted for protons or iron nuclei. By contrast, the mean free path for helium is much shorter than iron, such a composition arriving at Earth is expected to be dominated by heavy nuclei at the highest energies. As already mentioned, the highest energy UHECRs do appear to be heavier than protons (Abraham et al. 2010), although the precise composition is model- and calibration-dependent and hence remains uncertain.

5 CONCLUSIONS

We have explored the nucleosynthetic yield of the millisecond magnetar birth, using wind trajectories based on the force-free magnetosphere geometry from V14 (Figs 1 and 2) and parametrized model for the PNS neutrino cooling evolution from Roberts et al. (2012, Fig. 4). Our main conclusions are summarized as follows.

(i) Neutrino-heated winds from millisecond magnetars with rotation periods $P \sim 1$–10 ms produce heavy element abundance distributions that extend to higher atomic number than that from otherwise equivalent spherical winds with the same $Y_e(t)$ (Fig. 7). This increase in the neutron-to-seed ratio is driven mainly by the faster expansion rate in protomagnetar winds caused by the faster divergence of the area function and due to additional magnetocentrifugal acceleration (V14). For the fastest rotation periods, $P = 1$–2 ms, it is also driven by the lower value of Y_e resulting from centrifugal acceleration.

Unfortunately, a direct detailed comparison of our predicted abundances to data (e.g. in the Solar system or on metal-poor stars) is hindered by the larger uncertainties in the time evolution of Y_e in the wind during the PNS cooling phase.

(ii) The heaviest elements are synthesized by outflows emerging along flux tubes with latitude $\theta \approx \theta_{max}$, i.e. those in outflows that graze the closed zone and pass near the equatorial plane outside the light cylinder (Fig. 5). These fields lines also dominate the total mass budget of the wind due to their larger fraction of the total solid angle and, to a lesser degree, enhancements in the mass-loss rate per unit area due to centrifugal acceleration.

(iii) The total ejecta mass for $P = 2$–5 ms is greatly reduced, by a factor of $\gtrsim 10$, due to the small fraction of stellar surface threaded by the open magnetic flux as compared to a spherical wind (Thompson 2004). Such suppression in the outflow fraction could be a generic feature of PNS winds if strong, dynamically important magnetic fields are transient but ubiquitous, e.g. as would be the case if they are present only during the convective phases of the PNS cooling evolution. Such uncertainties, in addition to the uncertain Y_e evolution, make it challenging to place constraints on the birth rate of magnetars based on their nucleosynthesis abundances (Fig. 9). For the most rapidly rotating case $P = 1$ ms, the total mass-loss is instead enhanced by a factor of 3 over the spherical case due to additional magnetocentrifugal acceleration (Table 1).

(iv) Due to dependence of the charged particle process and weak r-process pattern on the magnetic field strength and rotation rate of PNSs, natural variations in these quantities between different core collapse events could contribute to the diversity of abundances observed on metal-poor stars (Fig. 10). This r-process site in the PNS phase (post-explosion) is notably distinct from that discussed in the context of MHD SNe (e.g. Winteler et al. 2012). The latter, which invoke low-Y_e ejecta, have the potential to produce a greater total r-process yield; however, such extreme magnetars are likely rarer than those discussed here due to the larger angular momentum of the stellar progenitor core required to produce a maximally spinning PNS versus the slower ~ 2–5 ms periods described here.

Additional diversity in the r-process abundances of protomagnetar winds, not considered in detail here, could result from variations in the magnetic inclination angle. Magnetic dissipation within the resulting striped wind could result in additional wind heating and concomitant entropy gain prior to seed formation, facilitating a heavier r-process than the aligned case focused on here.

(v) If protomagnetars are the central engines of GRBs, their relativistic jets should contain an order unity mass fraction of heavy nuclei with $\bar{A} \approx 100$. Subsequent particle acceleration in such a jet could produce UHECRs with a heavy composition (Abraham et al. 2010) and an energy spectrum that extends roughly a factor of 2 above the nominal GZK cut-off for protons or iron nuclei (Egorova et al. 2004). Better statistics and modelling of the UHECR energy spectrum, as well as a more firm measurement of the composition-dependent UHECR spectrum, is needed to test this prediction and its subtle differences with the normal proton-dominated model predictions.

REFERENCES

Abbasi R. U. et al., 2005, ApJ, 622, 910
Abbasi R. et al., 2011, Phys. Rev. Lett., 106, 141101
Abraham J. et al., 2010, Phys. Rev. Lett., 104, 091101
Arcones A., Montes F., 2011, ApJ, 731, 5
Arcones A., Janka H.-T., Scheck L., 2007, A&A, 467, 1227
Arnould M., Goriely S., Takahashi K., 2007, Phys. Rep., 450, 97
Arons J., 2003, ApJ, 589, 871
Banerjee P., Haxton W. C., Qian Y.-Z., 2011, Phys. Rev. Lett., 106, 201104
Beloborodov A. M., 2010, MNRAS, 407, 1033
Bucciantini N., Quataert E., Arons J., Metzger B. D., Thompson T. A., 2008, MNRAS, 383, L25
Burbidge E. M., Burbidge G. R., Fowler W. A., Hoyle F., 1957, Rev. Mod. Phys., 29, 547
Cameron A. G. W., 1957, AJ, 62, 9
Cardall C. Y., Fuller G. M., 1997, ApJ, 486, L111
Cerutti B., Beloborodov A. M., 2016, Space Sci. Rev., preprint (arXiv:1611.04331)
Cescutti G., Romano D., Matteucci F., Chiappini C., Hirschi R., 2015, A&A, 577, A139
Cyburt R. H. et al., 2010, ApJS, 189, 240
Duan H., Qian Y., 2004, Phys. Rev. D, 69, 123004
Duncan R. C., Shapiro S. L., Wasserman I., 1986, ApJ, 309, 141
Egorova V. P. et al., 2004, Nucl. Phys. B, 136, 3
Eichler D., Livio M., Piran T., Schramm D. N., 1989, Nature, 340, 126
Fang K., Kotera K., Olinto A. V., 2012, ApJ, 750, 118
Fernández R., Metzger B. D., 2013, MNRAS, 435, 502
Fischer T., Martínez-Pinedo G., Hempel M., Liebendörfer M., 2012, Phys. Rev. D, 85, 083003
Frankel S., Metropolis N., 1947, Phys. Rev., 72, 914
Freiburghaus C., Rosswog S., Thielemann F., 1999, ApJ, 525, L121
Fröhlich C. et al., 2006, ApJ, 637, 415
Fuller G. M., Fowler W. A., Newman M. J., 1982, ApJS, 48, 279
Gaensler B. M., Slane P. O., 2006, ARA&A, 44, 17
Goriely S., Bauswein A., Janka H.-T., 2011, ApJ, 738, L32
Goriely S., Bauswein A., Just O., Pllumbi E., Janka H.-T., 2015, MNRAS, 452, 3894
Greisen K., 1966, Phys. Rev. Lett., 16, 748
Guilet J., Müller E., 2015, MNRAS, 450, 2153
Hoffman R. D., Woosley S. E., Qian Y.-Z., 1997, ApJ, 482, 951
Honda S., Aoki W., Ishimaru Y., Wanajo S., Ryan S. G., 2006, ApJ, 643, 1180
Honda S., Aoki W., Ishimaru Y., Wanajo S., 2007, ApJ, 666, 1189
Horiuchi S., Murase K., Ioka K., Mészáros P., 2012, ApJ, 753, 69
Hotokezaka K., Piran T., Paul M., 2015, Nat. Phys., 11, 1042
Ji A. P., Frebel A., Chiti A., Simon J. D., 2016, Nature, 531, 610

Just O., Bauswein A., Pulpillo R. A., Goriely S., Janka H.-T., 2015, MNRAS, 448, 541

Kajino T., Otsuki K., Wanajo S., Orito M., Mathews G. J., 2000, in Oryu S., Ishikawa M., Kamimura S., eds, Few-Body Problems in Physics '99. Springer, New York, p. 80

Kasen D., Bildsten L., 2010, ApJ, 717, 245

Lai D., Qian Y.-Z., 1998, ApJ, 505, 844

Langanke K., Martínez-Pinedo G., 2000, Nucl. Phys. A, 673, 481

Lattimer J. M., Schramm D. N., 1974, ApJ, 192, L145

Lemoine M., Kotera K., Pétri J., 2015, J. Cosmol. Astropart. Phys., 7, 016

Lippuner J., Roberts L. F., 2015, ApJ, 815, 82

Lyubarsky Y., Kirk J. G., 2001, ApJ, 547, 437

Macias P., Ramirez-Ruiz E., 2016, preprint (arXiv:1609.04826)

Mamdouh A., Pearson J. M., Rayet M., Tondeur F., 2001, Nucl. Phys. A, 679, 337

Martin D., Perego A., Arcones A., Korobkin O., Thielemann F.-K., 2015, preprint (arXiv:1509.07628)

Martínez-Pinedo G., Fischer T., Lohs A., Huther L., 2012, Phys. Rev. Lett., 109, 251104

Mathews G. J., Bazan G., Cowan J. J., 1992, ApJ, 391, 719

Metzger B. D., Thompson T. A., Quataert E., 2007, ApJ, 659, 561

Metzger B. D., Quataert E., Thompson T. A., 2008a, MNRAS, 385, 1455

Metzger B. D., Thompson T. A., Quataert E., 2008b, ApJ, 676, 1130

Metzger B. D., Giannios D., Thompson T. A., Bucciantini N., Quataert E., 2011a, MNRAS, 413, 2031

Metzger B. D., Giannios D., Horiuchi S., 2011b, MNRAS, 415, 2495

Metzger B. D., Vurm I., Hascoët R., Beloborodov A. M., 2014, MNRAS, 437, 703

Meyer B. S., Mathews G. J., Howard W. M., Woosley S. E., Hoffman R. D., 1992, ApJ, 399, 656

Moller P., Sierk A. J., Ichikawa T., Sagawa H., 2016, Atomic Data and Nuclear Data Tables, 109, 1

Mösta P. et al., 2014, ApJ, 785, L29

Mösta P., Ott C. D., Radice D., Roberts L. F., Schnetter E., Haas R., 2015, Nature, 528, 376

Nishimura N., Takiwaki T., Thielemann F.-K., 2015, ApJ, 810, 109

Nishimura N., Sawai H., Takiwaki T., Yamada S., Thielemann F.-K., 2017, ApJ, 836, L21

Oda T., Hino M., Muto K., Takahara M., Sato K., 1994, At. Data Nucl. Data Tables, 56, 231

Otsuki K., Tagoshi H., Kajino T., Wanajo S.-y., 2000, ApJ, 533, 424

Panov I. V., Korneev I. Y., Rauscher T., Martínez-Pinedo G., Kelić-Heil A., Zinner N. T., Thielemann F., 2010, A&A, 513, A61

Perego A., Rosswog S., Cabezón R. M., Korobkin O., Käppeli R., Arcones A., Liebendörfer M., 2014, MNRAS, 443, 3134

Piro A. L., Kollmeier J. A., 2016, ApJ, 826, 97

Podsiadlowski P., Mazzali P. A., Nomoto K., Lazzati D., Cappellaro E., 2004, ApJ, 607, L17

Qian Y., Woosley S. E., 1996, ApJ, 471, 331

Qian Y.-Z., Wasserburg G. J., 2007, Phys. Rep., 442, 237

Qian Y.-Z., Vogel P., Wasserburg G. J., 1998, ApJ, 506, 868

Quimby R. M., Yuan F., Akerlof C., Wheeler J. C., 2013, MNRAS, 431, 912

Ripley J. L., Metzger B. D., Arcones A., Martínez-Pinedo G., 2014, MNRAS, 438, 3243

Roberts L. F., Woosley S. E., Hoffman R. D., 2010, ApJ, 722, 954

Roberts L. F., Reddy S., Shen G., 2012, Phys. Rev. C, 86, 065803

Roederer I. U., 2017, AJ, 835, 23

Roederer I. U., Cowan J. J., Karakas A. I., Kratz K.-L., Lugaro M., Simmerer J., Farouqi K., Sneden C., 2010, ApJ, 724, 975

Sawai H., Yamada S., 2016, ApJ, 817, 153

Sneden C., Cowan J. J., Gallino R., 2008, ARA&A, 46, 241

Spitkovsky A., 2006, ApJ, 648, L51

Stanek K. Z. et al., 2006, Acta Astron., 56, 333

Sumiyoshi K., Suzuki H., Otsuki K., Terasawa M., Yamada S., 2000, PASJ, 52, 601

Suwa Y., Tominaga N., 2015, MNRAS, 451, 282

Suzuki T. K., Nagataki S., 2005, ApJ, 628, 914

Takahashi K., Witti J., Janka H.-T., 1994, A&A, 286, 857

Takiwaki T., Kotake K., Suwa Y., 2016, MNRAS, 461, L112

Tamborra I., Raffelt G. G., Hüdepohl L., Janka H.-T., 2012, J. Cosmol. Astropart. Phys., 1, 013

Thielemann F.-K. et al., 2011, Prog. Part. Nucl. Phys., 66, 346

Thompson T. A., 2004, in Fryer C. L., ed., Astrophysics and Space Science Library, Volume 302, Stellar Collapse. Kluwer, Dordrecht, p. 175

Thompson T. A., 2007, in Sato K., Hisano J., eds, Energy Budget in the High Energy Universe. World Scientific Press, Singapore, p. 251

Thompson T. A., Burrows A., Meyer B. S., 2001, ApJ, 562, 887

Thompson T. A., Chang P., Quataert E., 2004, ApJ, 611, 380

Thompson T. A., Quataert E., Burrows A., 2005, ApJ, 620, 861

Timmes F. X., Swesty F. D., 2000, ApJS, 126, 501

Timokhin A. N., 2006, MNRAS, 368, 1055

Tsujimoto T., Yokoyama T., Bekki K., 2017, ApJ, 835, L3

Usov V. V., 1992, Nature, 357, 472

Vlasov A. D., Metzger B. D., Thompson T. A., 2014, MNRAS, 444, 3537

Wahl A. C., 2002, Technical Report LA-13928, Systematics of Fission-Product Yields. Los Alamos National Laboratory, Los Alamos, NM

Wallner A. et al., 2015, Nat. Commun., 6, 5956

Wanajo S., Sekiguchi Y., Nishimura N., Kiuchi K., Kyotoku K., Shibata M., 2014, ApJ, 789, L39

Waxman E., 1995, Phys. Rev. Lett., 75, 386

Wehmeyer B., Pignatari M., Thielemann F.-K., 2015, MNRAS, 452, 1970

Wheeler J. C., Yi I., Höflich P., Wang L., 2000, ApJ, 537, 810

Winteler C., Käppeli R., Perego A., Arcones A., Vasset N., Nishimura N., Liebendörfer M., Thielemann F.-K., 2012, ApJ, 750, L22

Woods P. M., Thompson C., 2006, in Lewin W. H. G., van der Klis M., eds, Compact Stellar X-ray Sources. Cambridge Univ. Press, Cambridge, p. 547

Woosley S. E., 2010, ApJ, 719, L204

Woosley S. E., Bloom J. S., 2006, ARA&A, 44, 507

Woosley S. E., Hoffman R. D., 1992, ApJ, 395, 202

Woosley S. E., Wilson J. R., Mathews G. J., Hoffman R. D., Meyer B. S., 1994, ApJ, 433, 229

Wu M.-R., Fischer T., Huther L., Martínez-Pinedo G., Qian Y.-Z., 2014, Phys. Rev. D, 89, 061303

Wu M.-R., Fernández R., Martínez-Pinedo G., Metzger B. D., 2016, MNRAS, 463, 2323

Zatsepin G. T., Kuzmin V. A., 1966, J. Exp. Theor. Phys. Lett., 4, 114

This paper has been typeset from a TEX/LATEX file prepared by the author.